New magnetic data indicate successive ridge jumps and rotations of seafloor spreading in the South China Sea

Qingsheng Guan[1,2,3], Tao Zhang[2,3*], Brian Taylor[4], Jinyao Gao[2,3], Jiabiao Li[2,3*]

[1]Collaborative Innovation Center of South China Sea Studies and School of Geographic and Oceanographic Sciences, Nanjing University, Nanjing, China.

[2]Second Institute of Oceanography, Ministry of Natural Resources, Hangzhou, China.

[3]Key Laboratory of Submarine Geosciences, Ministry of Natural Resources, Hangzhou, China.

[4]School of Ocean and Earth Science and Technology, University of Hawaii at Manoa, Honolulu, USA.

Corresponding authors: Jiabiao Li and Tao Zhang,

(**jbli@sio.org.cn;** tao_zhang@sio.org.cn)

Key Points:

- We present a new high-resolution oceanic crustal age model of the South China Sea.
- Seafloor spreading in the South China Sea is characterized by successive ridge jumps and counterclockwise rotations of seafloor spreading.
- Frequent ridge jumps and rotations of seafloor spreading may be dynamic responses to the plate tectonics around the South China Sea.

Abstract

New shipborne surveys provide a closely spaced magnetic anomaly dataset covering the East Subbasin (ESB) of the South China Sea (SCS). Magnetic anomalies of seafloor spreading are identified using the dataset supplemented with previous data and age constraints from recent International Ocean Discovery Program Expeditions 349 and 367/368 holes. We present a high-resolution oceanic crustal age model and associated magnetic lineations of the ESB based on identified magnetic anomaly picks. Seafloor spreading in the ESB initiated at ~30 Ma (C11n) and terminated at ~16 Ma (C5Br). The spreading direction has experienced a gradual counterclockwise rotation between C6Cr and C5Er and a significant counterclockwise rotation at C5Dr. The spreading rotations reorganized the orientation and segmentation of the spreading ridge, resulting in the formation of a series of S-shaped fracture zones. The interpretation of the magnetic lineations reveals that three southward ridge jumps occurred at C9r, C8n, and C7n and a synchronous jump occurred at C5Dr. Three southward ridge jumps contributed to a total difference of ~184 km in the distance between the two flanks and left the paired magnetic lineations C10r–C7r on the present-day north flank. The synchronous jump caused the spreading ridge to rotate rapidly counterclockwise and obliquely intersect the existing seafloor. We postulate that these ridge jumps and rotations are common processes during seafloor spreading reorientation and are dynamic responses to the plate or microplate tectonics around the SCS.

1 Introduction

The South China Sea (SCS) is the largest marginal basin in Southeast Asia and has experienced an almost complete Wilson cycle since the early Cenozoic. Studies of the SCS can provide important information for reconstructing the Cenozoic tectonics of Southeast Asia and improve the understanding of the evolution of marginal basins. Although the seafloor spreading history and geodynamics of the SCS have been extensively studied, some key issues remain controversial or unclear: first, the debates about the age of seafloor spreading, such as ~30–16 Ma (Briais et al., 1993; Taylor & Hayes, 1983), ~32–20.5 Ma (Barckhausen et al., 2004, 2014), and ~33–15 Ma (Li et al., 2014); second, the asymmetric spreading processes during the early spreading stage (Briais et al., 1993; Ding et al., 2018); third, the locations and trends of the major fracture zones in the SCS (Ruan et al., 2016; Sibuet et al. 2016; Yao, 1995); and finally, several potential geodynamic mechanisms for the opening of the SCS, including the slab pull model (Holloway, 1982; Taylor & Hayes, 1980, 1983), Indochina extrusion model (Briais et al., 1993; Tapponnier et al., 1982). A robust crustal age model and associated magnetic lineations could provide crucial insights into the above major unsolved controversies. However, due to intense post-spreading volcanism and lack of microfossil or radiometric ages, previous magnetic lineation patterns based on relatively sparse magnetic data have been debated (e.g., Barckhausen et al., 2004, 2014; Briais et al., 1993; Li et al., 2014; Taylor & Hayes, 1983; Zhang et al., 2012).

In this paper, we use recently collected sea surface magnetic data to establish a set of high-resolution magnetic lineations and a new crustal age model for the East Sub-basin (ESB) of the SCS. Based on the magnetic anomalies, we identify successive ridge jumps and describe the detailed jumping processes of these spreading ridges. Combined analyses of magnetic anomalies, vertical gravity gradient (VGG), and geomorphic features, we determine the locations and trends of the major fracture zones in the SCS. On the basis of the magnetic lineations, we decipher the continuous counterclockwise

rotations of seafloor spreading. We further discuss the implications of seafloor spreading rotations for the geodynamic processes of the evolution of the SCS.

2 Geological Background

The SCS is situated at the junction of the Eurasian, Indo-Australia, and Philippine plates (Figure 1). Its surroundings include three major types of continental margins. The northern and southern parts of the SCS are passive rift continental margins. The eastern part is bounded by the Manila Trench, where the SCS slab subducts 400~500 km beneath the Philippine plate (Wu et al, 2016). The western part is bounded by a strike-slip fault zone, along which Indochina was extruded by the collision between the Indian and Eurasian plates (Leloup et al., 2001; Tapponnier et al., 1982, 1990).

The oceanic basin of the SCS has been divided into the ESB, the Southwest Subbasin (SWSB), and the Northwest Subbasin (NWSB). The ESB is separated from the SWSB and the NWSB by a major Zhongnan fracture/fault zone (Sibuet et al., 2016; Yao, 1995). However, the location and trend of the Zhongnan fracture/fault zone are still controversial. Based on morphological and seismic data, Yao (1995) proposed that the Zhongnan fault is an N–S-trending fault that extends along 116°E northward to south China margin and southward to Borneo. Similarly, on the basis of swath-bathymetric data, Sibuet et al. (2016) postulated that the Zhongnan fault is a generally NNW–SSE-trending fracture zone, which contain a series of parallel fracture zones. Ruan et al. (2016) suggested that the Zhongnan fault is an NW–SE-trending fracture zone near 116°E with a width of 40–60 km based on wide-angle seismic profiles.

2.1 Crustal age models of the SCS

The oceanic crustal age of the SCS has been estimated by the identification of magnetic anomalies and dating from the International Ocean Discovery Program (IODP). Three major age models have been established based on magnetic data from the SCS. Following Taylor and Hayes (1980, 1983), Briais et al. (1993) suggested that the SCS spreading occurred from ~30 Ma to ~16 Ma (revised based on the geomagnetic

97 polarity time scale (GPTS) of Gee and Kent (2007)). By reinterpreting the magnetic
98 anomalies from different magnetic data, Barckhausen et al. (2004, 2014) proposed that
99 seafloor spreading in the SCS initiated at 32 Ma and ceased at 20.5 Ma. Li et al. (2014)
100 jointly analyzed the deep-tow magnetic data and IODP Expedition 349 cores and
101 estimated that the seafloor spreading duration in the SCS was ~33–15 Ma.
102 IODP Expeditions 349 and 367/368 drilled at the northern continent-ocean
103 boundary (COB) and near the fossil ridge in 2014 and 2017, respectively (Figure 1).
104 On the northern COB, Site U1500 and Site U1502 from IODP Expeditions 367/368
105 were cored into the igneous basement rocks that were directly overlain by late
106 Oligocene (~27 Ma) and early Oligocene (~30 Ma) sediments, respectively (Larsen et
107 al., 2018; Sun et al., 2018). The core at Site U1435 from IODP Expedition 349
108 penetrated through a breakup unconformity (~33 Ma), although it did not reach the
109 igneous basement (Li et al., 2015). In the area close to the fossil ridge, Sites U1431,
110 U1433, and U1434 from IODP Expedition 349 cored into the igneous basement, and
111 $^{40}Ar/^{39}Ar$ dating of the three sites yielded ages of ~15 Ma, ~17.3 Ma, and ~16.3 Ma,
112 respectively (Koppers, 2014). However, the age of Site U1431 is slightly younger than
113 the age of the overlying sedimentary layer, which may have resulted from the basalt
114 intruding the already deposited sediments after the cessation of spreading (Sibuet et al.,
115 2016).

116 **2.2 Seafloor spreading in the SCS**

117 The opening of the SCS basin from the northeast to the southwest experienced two
118 stages. The first stage was initiated by the opening of the ESB and the NWSB, but
119 seafloor spreading of the NWSB lasted only ~2–2.6 Ma (Briais et al., 1993; Zhang et
120 al., 2012). In the ESB, possible ridge jumps are observed and cause asymmetry in the
121 geometry and magnetic anomalies (Briais et al., 1993; Ding et al., 2018). However,
122 only the ridge jump at C7/C6C has been previously identified by magnetic data
123 (Barckhausen et al., 2004, 2014; Briais et al., 1993; Li et al., 2014). This ridge jumped
124 southward by approximately 20 km (Li et al., 2014), contributing to a ~40 km difference

between the northern and southern flanks. After the ridge jump, seafloor spreading propagated progressively southwestward, and the second stage began (Li et al., 2012).

Li et al. (2002) analyzed the trends of the fracture zones in the ESB and suggested that the spreading direction of the SCS might have been N137° during the late spreading stage. Recently, Sibuet et al. (2016) proposed that the SCS experienced three spreading directions: N175°, N165°, and N145°, based on magnetic lineations and the seafloor fabric. This view is supported by the major axis orientations of the intraplate seamounts in the SCS (Fan et al., 2017).

2.3 Geodynamic models of the SCS opening

Two end-members driving force models have been proposed for the SCS opening, involving the slab pull model (Holloway, 1982; Taylor & Hayes, 1980, 1983) and Indochina extrusion model (Briais et al., 1993; Tapponnier et al., 1982, 1990). In slab pull model, the southward subduction of the Proto-SCS (PSCS) drove the rifting and opening of the SCS. Following the detachment of the Dangerous Grounds and North Palawan blocks from the South China block, seafloor spreading in the SCS initiated (Zahirovic et al., 2014). Seafloor spreading in the SCS ceased when these blocks collided with Borneo (Taylor & Hayes, 1980, 1983).

Alternatively, the Indochina extrusion model hypothesizes that several hundred kilometers of southeastward extrusion of Indochina along the Ailaoshan-Red River shear zone (ARRSZ) triggered the opening of the SCS in a pull-apart manner (Briais et al., 1993; Tapponnier et al., 1982; 1990). The large-scale left-lateral strike-slip movements along the ARRSZ were limited to ~35–17 Ma based on the cooling ages of metamorphic rocks from the ARRSZ (Gilley et al., 2003; Leploup et al., 2001; Schärer et al., 1990). The offshore prolongation of the ARRSZ extends southward along the Vietnamese margin, and was named as East Vietnam Boundary Fault Zone (EVBFZ) (Fyhn et al., 2009a, 2009b). The left-lateral movements along the EVBFZ ceased around the middle Oligocene due to a temporary change from transtension to transpression (Fyhn et al., 2009b).

3 Data and Methods

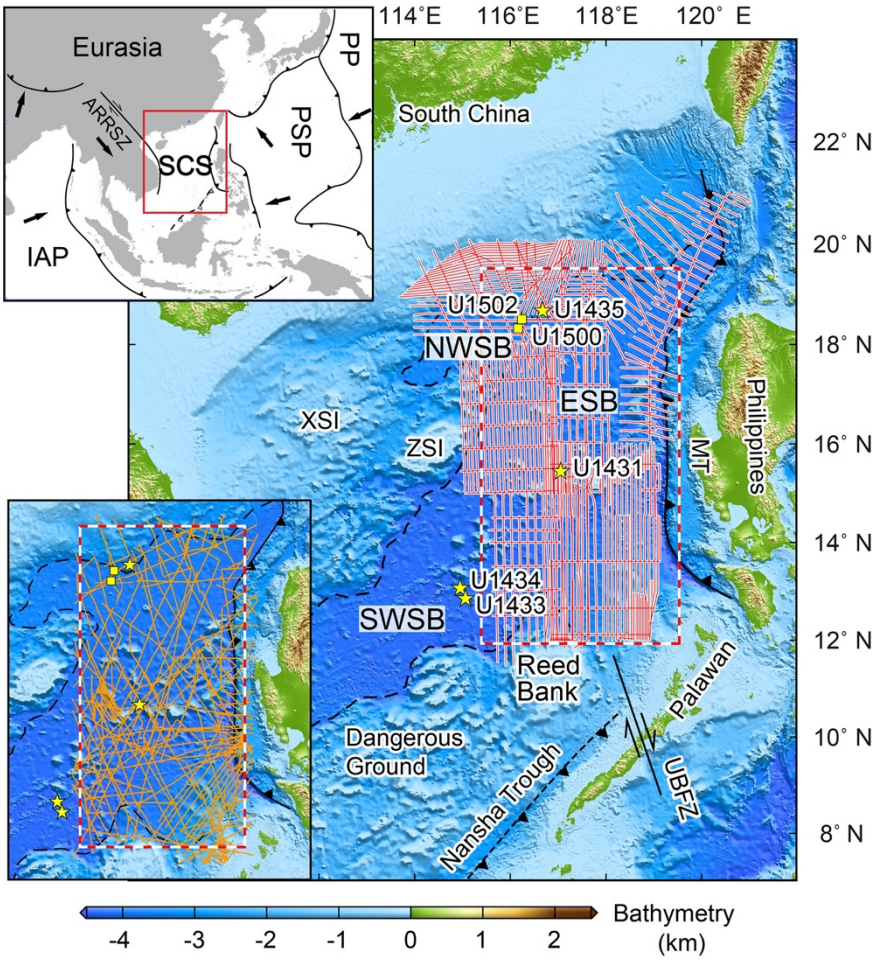

Figure 1. Location of the SCS and tracks of magnetic profiles. Red box marks the research area of this study. Red lines indicate sea surface magnetic tracks. Yellow stars indicate the drilling sites of IODP Expedition 349 (Li et al., 2015). Yellow squares indicate the drilling sites of IODP Expeditions 367 and 368 (Sun et al., 2018). Black dashed lines indicate the continent-ocean boundary determined from the vertical gravity gradient (Sandwell et al., 2014). The upper left inset shows the plate tectonic setting. The lower left inset shows supplementary magnetic tracks obtained from the National Centers for Environmental Information. XSI, Xisha Islands; ZSI, Zhongsha Islands; ARRSZ, Ailaoshan-Red River Shear Zone; MT, Manila Trench; UBFZ, Ulugan Bay Fault Zone; IAP, Indo-Australian Plate; PSP, Philippine Sea Plate; PP, Pacific Plate.

166 The high-resolution sea surface magnetic data for the ESB, composed of 389
167 magnetic profiles with a total length of 57,600 km, were collected between 1999 and
168 2014 (Figure 1). The magnetic data have denser sampling, better navigation, and greater
169 geographic coverage than previous data. The trend of most track lines is N–S, which is
170 consistent with the spreading direction of the SCS. The mean spacing of the track lines
171 is approximately 10 km. A cesium and/or proton precession magnetometer was towed
172 behind a research vessel at a distance of 2.5–3 times the length of the vessel during the
173 investigations. The magnetic data are processed with the following three steps (Gao &
174 Liu, 2014). First, the magnetic data are corrected for diurnal variations with the data
175 from nearby temporary magnetic observatories. Second, the magnetic anomaly is
176 calculated by removing the international geomagnetic reference fields (IGRF)
177 (Thébault et al., 2015). Finally, the magnetic anomaly of each profile is shifted by a
178 constant value to minimize the crossover errors according to the least-squares criterion.
179 The root-mean-square error of the processed magnetic data at crossover points is 12.9
180 nT.
181 The collected sea surface magnetic data are combined with supplementary data
182 from the National Centers for Environmental Information to constitute the final
183 magnetic dataset (Figure 1). After applying a constant shift to each profile, the root-
184 mean-square error of the magnetic dataset at crossover points is 19 nT. A magnetic
185 anomaly map of the ESB is produced by gridding the magnetic dataset using the
186 Generic Mapping Tools software (Wessel et al., 2019) (Figure 3). Meanwhile, we also
187 determine the COB of the SCS based on the version 28 of VGG from Sandwell et al.
188 (2014).
189 We select the nearly N–S-trending profiles from the magnetic dataset to identify
190 magnetic anomalies. Magnetic anomalies are identified through the stacking of
191 magnetic profiles, identification of the stacked profiles, and identification of each
192 profile. The magnetic anomalies on each profile with relatively large amplitudes and
193 similar shapes are assumed to be caused by the same geomagnetic reversals. The

194 magnetic profiles are stacked based on the selected magnetic anomalies associated with
195 the same geomagnetic reversals (Figures S2 and S3). Along the stacked profile, the
196 signals of the Earth's magnetic field reversals are enhanced, and signals generated by
197 local tectonic and magmatic activities are suppressed (Zhang et al., 2019).

198 We perform forward modeling using the software MODMAG (Mendel et al., 2005)
199 under the constraints of dating from the IODP Expeditions 349, 367, and 368 sites
200 (Koppers, 2014; Li et al., 2015; Sun et al., 2018). The GPTS model of Gee and Kent
201 (2007) is used in the forward modeling. The magnetization of the magnetic sources is
202 assumed to be 5 A/m. The thickness of the magnetic layer is assumed to be 0.7 km to
203 match the amplitudes of the magnetic anomalies. The contamination coefficient R is
204 set to be 0.7 ($0<R<1$, with 1 for no contamination) to better match the shapes of the
205 magnetic anomalies. The mean ambient declination and inclination of the fossil ridges
206 at 117°E are -1.5° and 17.5°, respectively.

207 The shapes and amplitudes of the magnetic anomalies along the synthetic profile
208 are visually compared to those of the stacked profile to determine the best-fit
209 geomagnetic polarity reversal sequences. The coherent magnetic anomaly picks of each
210 profile are then identified based on the sequences of the stacked profile.

4 Results

4.1 Crustal age model

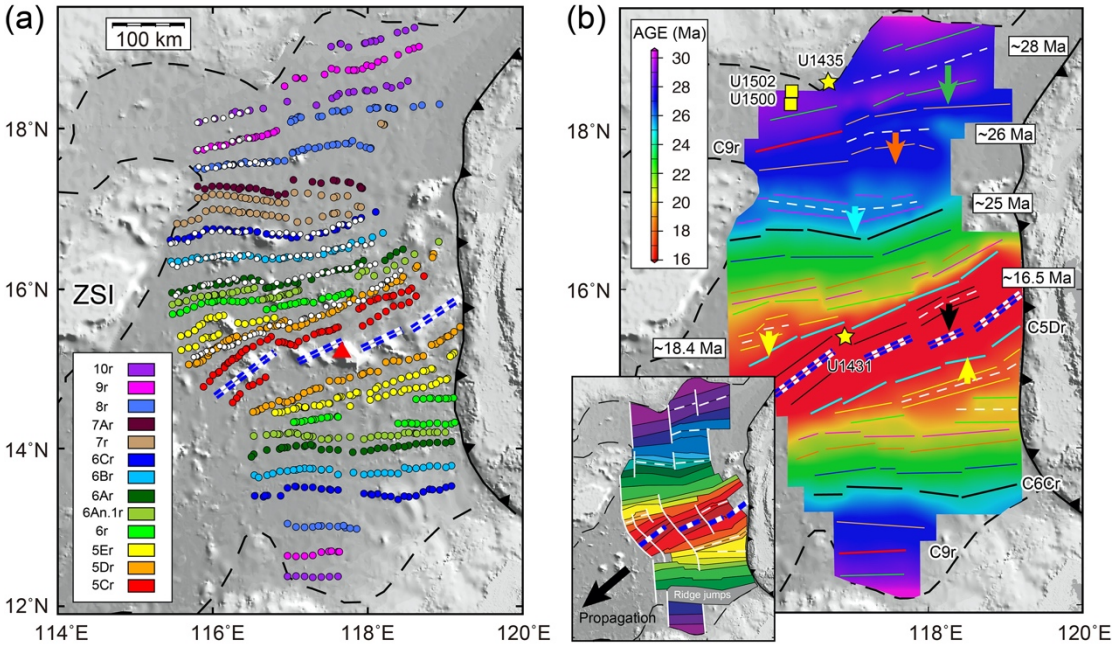

Figure 2. Magnetic anomaly picks and oceanic crustal ages in the ESB. (a) Solid circles indicate the magnetic anomaly picks identified from the magnetic profiles. Open circles indicate the magnetic anomaly picks on the south flank rotated onto the north flank. Blue double dashed lines indicate possible locations of the fossil ridges. The background is shaded topography (Tozer et al., 2019). Red triangle is where the spreading directions and rates of the ESB are computed in section 4.4. (b) Oceanic crustal ages of the ESB inferred from magnetic lineations. White dashed lines mark the locations of the ridge jumps. The inset indicates the postulated tectonic evolution of the ESB. White lines in the inset indicate potential fracture zones.

We identify 13 reverse polarity chrons (C10r–C5Cr) along magnetic anomaly profiles in the ESB (Figure 2a). The oldest magnetic anomaly close to the northern COB is C11n (Figure S2a), as originally identified by Taylor and Hayes (1980, 1983), indicating that seafloor spreading in the ESB initiated at C11n (~30 Ma). The magnetic lineation pattern consists of 856 magnetic anomaly picks, which is several times the numbers in previously studies (Barckhausen et al., 2004, 2014; Briais et al., 1993; Li et

al., 2014; Taylor et al., 1983). More picks and smaller mean spacing between picks along the isochrones improve the resolution of the magnetic lineation pattern.

Each magnetic lineation is assigned an age based on the middle of the associated polarity epoch of the GPTS. The magnetic lineations are then associated with crustal ages between ~30 Ma and 17 Ma. The distance between the youngest magnetic lineations C5Cr (17 Ma) and the fossil ridge is ~22 km. Given a half spreading rate of 22.8 mm/yr (between C6Ar and C5Dr) (Figure 5b), seafloor spreading ceased at ~16 Ma. An oceanic crustal age grid (0.5′×0.5′) of the ESB is then created using the minimum curvature method (Figure 2b).

4.2 Identification of ridge jumps

The two flanks of the fossil ridge in the ESB exhibit two conspicuous negative magnetic anomalies (M1 and M2 in Figure 3) which are conjugated to each other (Briais et al., 1993; Li et al., 2014; Taylor & Hayes, 1980, 1983). According to the numbers and distribution of magnetic lineations, the oceanic domain between M1/M2 and the COBs on both flanks can be divided into the eastern and western parts along the magnetic lineation offset near 117°E in the north flank and the magnetic lineation offset near 118°E in the south flank (Figures 3a and 3b).

Each western part of the two flanks contains three positive magnetic anomalies, although the magnetic lineation close to the COB on the south flank is blurred. The profiles crossing these magnetic anomalies show a conjugate anomaly pattern. The distances between M1/M2 and the COBs on both flanks are also roughly equal. These observations indicate that the sequence of magnetic anomalies in the western parts is generated by normal oceanic crust accretion. We interpret the first three positive magnetic anomalies as C10r, C9r, and C8r under the constraints of age from hole U1502 (Sun et al., 2018). In addition, there are two anomalous magnetic anomalies between anomalies C8 and C6Cr on the north flank, but they are missing in the conjugate area on the south flank (Figures 3a and 3b). We infer that a southward ridge jump may have occurred between anomalies C8r and C6Cr. Based on forward modeling, we interpret

two anomalous magnetic anomalies as paired C7r caused by the ridge jump at C7n (~25 Ma).

In the eastern part, the north flank between M1 and the northern COB has a width of ~190 km and contains five positive magnetic lineations (Figure 3a). The south flank between M2 and the southern COB has a width of ~45 km, and there are no prominent and continuous magnetic lineations (Figure 3b). These differences between the two flanks indicate asymmetric seafloor spreading during the early spreading stage. The asymmetric spreading rates cannot explain the absence of magnetic lineations between M2 and the southern COB on the south flank. Therefore, we prefer to explain the asymmetric seafloor spreading via ridge jumps. We postulate that ridge jumps have resulted in the magnetic anomalies between M2 and the southern COB remaining on the present-day north flank. This interpretation means that the five magnetic lineations on the present-day north flank were generated on both flanks in the eastern part. A plausible explanation is that the eastern and western parts contemporaneously initiated seafloor spreading at C11n (~30 Ma) and that the spreading ridge in the eastern part jumped southward twice (see section 5.2 for details).

In the area close to the fossil ridge, a magnetic lineation with a strong amplitude (C5Dr) obliquely intersects two magnetic lineations (C5Er) on the north flank (Figure 3c), which indicates that a ridge jump may have occurred and been accompanied by a reorientation of the spreading ridge. We identify the strong magnetic lineation as C5Dr based on microfossil dating from hole U1431 (Li et al., 2015). Although complex tectonism and intense post-spreading volcanism in this area have complicated the magnetic anomalies (Figure 3c), we still tentatively speculate that a ridge jump occurred after anomaly C5Er, associated with the synchronous reorientation of the spreading ridge. This type of reorientation results from a large and rapid change in the direction of plate motion, which also occurred in the Woodlark Basin and Pacific-Farallon spreading center (Goodliffe et al., 1997). In the latest spreading stage, an instantaneous ridge jump may have occurred after anomaly 5Cr to the east of 117.5°E

(Figure 3c). The ridge segment jumped southward to the location of the present-day fossil ridge, generating a larger offset near 117.5°E. These magnetic anomaly interpretations are supported by the seafloor fabric from the bathymetry of the fossil ridge region (Hsu et al., 2019; Li et al., 2002).

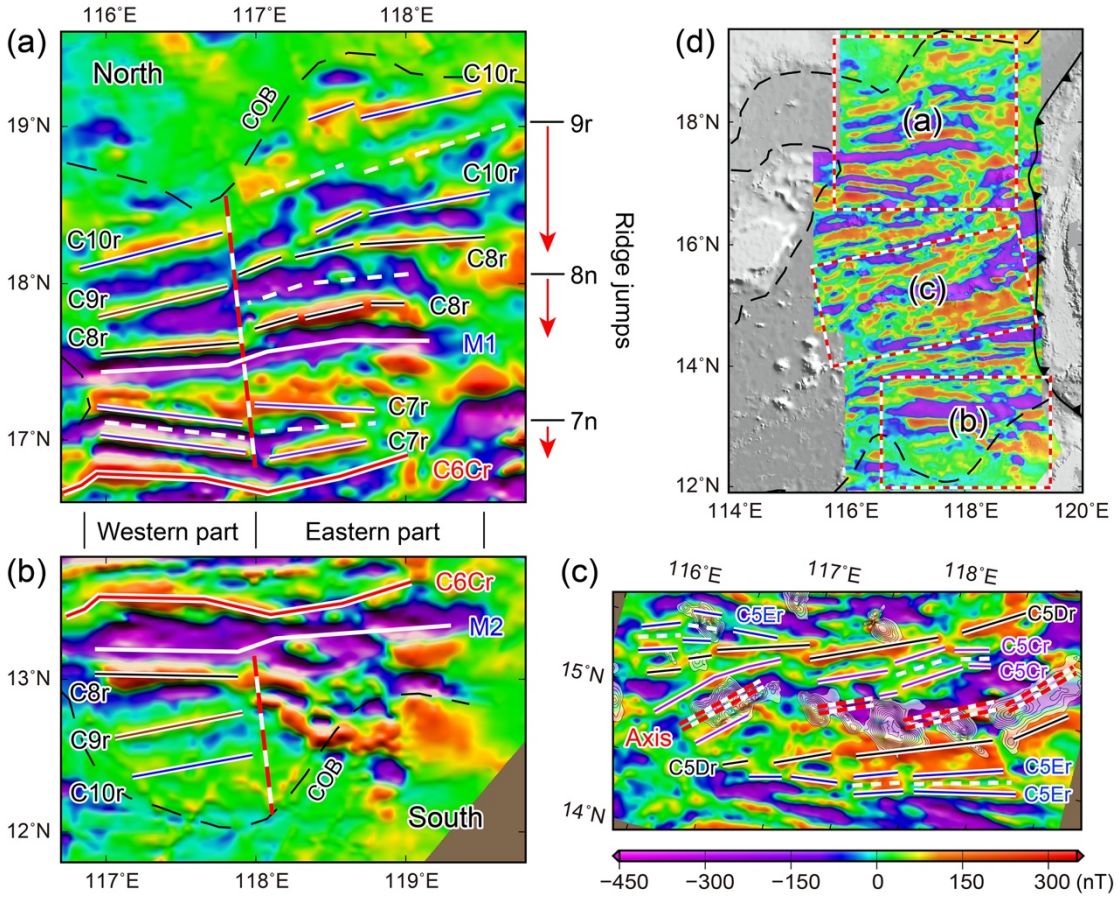

Figure 3. Magnetic anomalies in the ESB and identifications of ridge jumps. (a) and (b) Magnetic anomalies of the conjugate areas close to the COBs on the north and south flanks, respectively. Colored lines indicate magnetic lineations between C10r and C6Cr. Red dashed lines indicate the fracture zones. White dashed lines indicate the locations of the ridge jump. M1 and M2 are a pair of conjugate negative magnetic anomalies with large amplitudes. (c) Magnetic anomalies near the fossil ridge. Double dashed lines indicate the fossil ridge. Black contour areas represent post-spreading seamounts. (d) Magnetic anomalies in the ESB. Red boxes indicate the areas of (a), (b), and (c) in the figure.

4.3 Euler poles

We calculate the finite rotation parameters by fitting the conjugate magnetic anomaly picks using the software GPlates (Müller et al., 2018) (Table 1). The fitting is performed using algorithms based on the work of Hellinger (1981) and Chang (1988). During the calculation, a grid search is first carried out for the finite rotation parameters, and the routine of the GPlates then refines the result. For each isochron, we compute 15 iterations or continue until the amoeba residual is less than 10^{-10} in GPlates to obtain the finite poles. We do not calculate the finite poles of the isochrons C5Er, C6r, and C7r, because the ridge jumps destroyed the magnetic lineations and caused the paired magnetic lineations on one flank. To obtain the spreading directions and spreading rates, we calculate two sets of stage poles based on these finite poles (Table 2). One set consists of the stage poles of the north flank obtained by fixing the South China block on the north flank of the SCS and moving the blocks on the south flank. The other set consists of the stage poles of the south flank obtained by the opposite relative movement.

The uncertainty ellipses cannot be calculated in GPlates due to the short isochrons and the lack of large offsets in all isochrons. To test the fitting of each isochron, we rotate the magnetic anomaly picks on the south flank to the north flank based on the rotation parameters (Figure 2a). The fixed picks show good fits with rotated picks, and some small offsets on conjugate isochrons, which are important fitting constraints, also match well. Moreover, the locations of the calculated finite poles are very close to those of Briais et al. (1993) (Figure 4). Therefore, the finite poles obtained in this study are reliable.

Table 1. Finite pole parameters.

Anomalies	Age (Ma)	Longitude (°)	Latitude (°)	Angle (°)
C5Dr	17.95	107.17	3.89	3.83
C6Ar	21.54	86.97	-0.49	4.20
C6Br	23.21	83.19	0.01	4.84
C6Cr	24.42	78.13	-0.01	5.19

C8r	26.79	91.71	8.51	10.77
C9r	28.13	82.76	6.12	9.24
C10r	29.07	88.07	7.58	12.07

Positive longitudes and latitudes correspond to the eastern and northern hemispheres, respectively.

Table 2. Stage pole parameters.

Anomalies	Age span (Ma)	North flank			South flank		
		Longitude (°)	Latitude (°)	Angle (°)	Longitude (°)	Latitude (°)	Angle (°)
End–C5Dr	1.95	107.17	3.89	1.92	107.17	3.89	-1.92
C5Dr–C6Ar	3.59	22.09	-13.39	0.74	21.76	-9.58	-0.74
C6Ar–C6Br	1.67	60.00	2.03	0.35	60.23	3.93	-0.35
C6Br–C6Cr	1.21	29.00	-2.14	0.28	28.99	1.79	-0.28
C6Cr–C8r	2.37	103.27	16.63	2.98	104.57	14.38	-2.98
C8r–C9r	1.34	-46.57	-19.53	1.11	-45.91	-12.38	-1.11
C9r–C10r	0.94	104.38	13.36	1.50	105.15	9.91	-1.50

Positive longitudes and latitudes correspond to the eastern and northern hemispheres, respectively.

We plot the seven finite poles in Figure 4 from C10r (29.07 Ma) to C5Dr (17.95 Ma). Overall, the finite poles are located to the southwest of the SCS, conforming with the V shape of the oceanic basin. The poles for C10r, C9r, and C8r are located to the west of the SCS, corresponding to the westward propagation of the basin during the early spreading stage. The poles for C6Cr, C6Br, and C6Ar migrated toward the southwest, which indicates that the propagation changed to the southwest corresponds to the opening of the SWSB. The pole for C5Dr jumped eastward to be closer to the basin, reflecting the major change in the spreading direction during the late spreading stage.

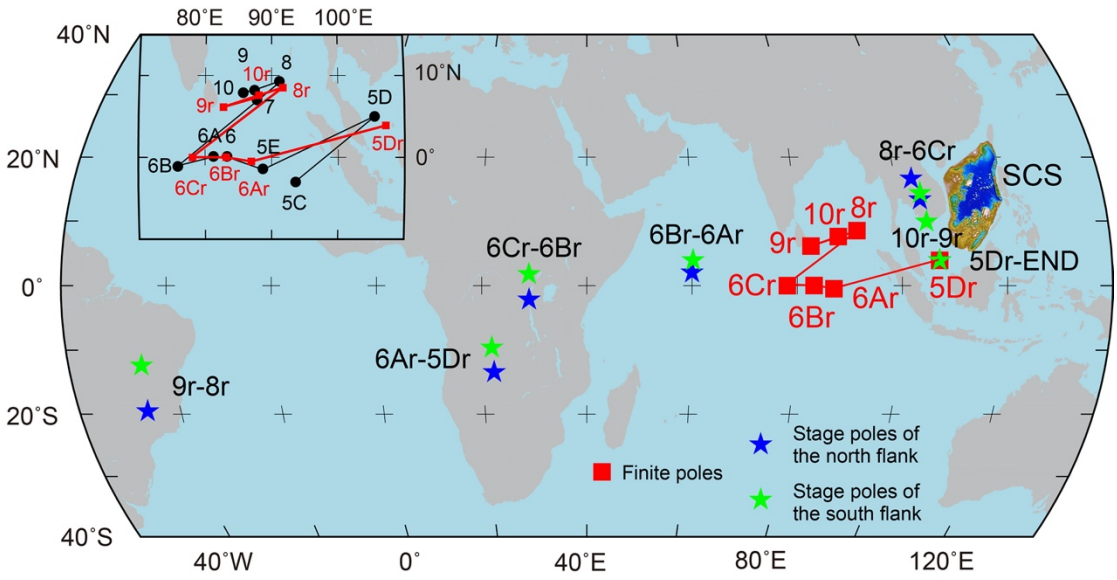

334

335 **Figure 4**. Locations of the finite poles and stage poles. Red squares indicate the finite
336 poles. Blue stars indicate the stage poles of seafloor spreading in the north flank, and
337 green stars indicate the stage poles of seafloor spreading in the south flank. In the inset,
338 our finite poles (red squares) are compared with those (black dots) of Briais et al. (1993).

339 **4.4 Spreading directions and spreading rates**

340 We compute the spreading directions and spreading rates of the north and south
341 flanks based on two sets of stage poles (Table 3). The average spreading directions
342 show that the initial spreading direction of the ESB was ~N166°, and then the direction
343 rotated clockwise at C9r from ~N166° to ~N175° (Figure 5a). After C6Cr, the
344 spreading direction began to gradually and continuously rotate counterclockwise until
345 C5Dr. A significant direction rotation occurring at C5Dr and the direction rotated
346 counterclockwise from ~N170° to ~N134°. The average spreading rates show that the
347 initial full spreading rate of the ESB was ~80 mm/yr, followed by a sharp decrease to
348 ~49 mm/yr at C9r (Figure 5b). From C9r to C6Br, the spreading rate varied between
349 ~49 mm/yr and 64 mm/yr. Between C6Br and C5Dr, the spreading rate decreased to a
350 relatively slow rate, between 40 mm/yr and 46 mm/yr. Since C5Dr, the spreading rate
351 increased to ~58 mm/yr.

352 Based on the spreading directions and spreading rates, seafloor spreading in the
353 ESB can be divided into three stages (Figure 5). In stage 1 (C10r–C6Br), the overall

354 spreading direction trended nearly N–S, except for the initial spreading direction
355 (between C10r and C9r). The spreading rate was an intermediate spreading rate
356 (average rate: ~61 mm/yr). In stage 2 (C6Br–C5Dr), the spreading directions were close
357 to the NNW–SSE direction, corresponding to a slow spreading rate (average rate: ~44
358 mm/yr). In stage 3 (C5Dr–cessation of seafloor spreading), the spreading direction was
359 NW–SE. The spreading rate increased again to an intermediate spreading rate (average
360 rate: ~58 mm/yr).

361 **Table 3.** Spreading directions and half spreading rates of the ESB

Anomalies	Age interval (Ma)	North flank		South flank	
		Spreading directions (°)	Half spreading rate (mm/yr)	Spreading directions (°)	Half spreading rate (mm/yr)
End–C5Dr	16.00–17.95	131.7	28.9	135.6	28.8
C5Dr–C6Ar	17.95–21.54	168.4	22.7	172.2	22.8
C6Ar–C6Br	21.54–23.21	171.8	20.0	176.0	20.0
C6Br–C6Cr	23.21–24.42	177.4	25.9	181.5	25.9
C6Cr–C8r	24.42–26.79	178.4	32.1	188.4	32.0
C8r–C9r	26.79–28.13	171.0	24.7	178.7	24.7
C9r–C10r	28.13–29.07	160.4	40.0	171.3	39.9

362 The directions and rates of seafloor spreading were calculated for point (red triangle in Figure 2a)
363 on the fossil ridge based on the two sets of stage poles.

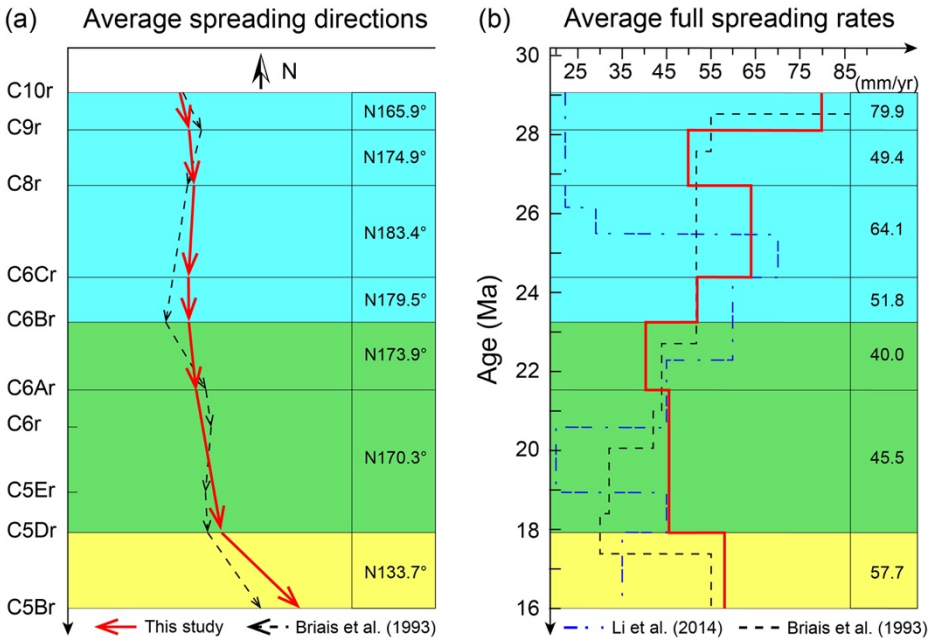

Figure 5. (a) Average spreading directions of the north and south flanks in the ESB. Red lines with arrows indicate the average spreading directions calculated in this study, and black dashed lines with arrows indicate the spreading directions from Briais et al. (1993). (b) Average spreading rates of the north and south flanks in the ESB. Red lines indicate the average spreading rates calculated in this study. Black and blue dotted lines indicate the spreading rates from Briais et al. (1993) and Li et al. (2014), respectively. Three shaded areas indicate stage 1, stage 2, and stage 3 of seafloor spreading.

The initial spreading rate in the ESB was up to ~80 mm/yr, potentially supporting rapid extension in the SCS margin during breakup (Ding et al., 2019; Larsen et al., 2018). The rapid extension within a relatively short period (<10 Ma) resulted in the generation of enhanced and localized magma associated with asthenospheric upwelling and decompression melting (Ding et al., 2019; Larsen et al., 2018). Nirrengarten et al. (2020) also suggested that the magmatism during initial breakup heated the pre-rift sediments to temperatures as high as 200℃. Therefore, thermal erosion related to the magma penetrating the lithosphere may have weakened the thinned lithosphere and promoted rapid rift-to-drift transition in the SCS.

5 Discussion

5.1 Comparison with previous crustal age models

Our crustal age model suggests that seafloor spreading in the ESB initiated at ~30 Ma (Figure 2), which is similar to the age proposed by Taylor and Hayes (1980,1983) and Briais et al. (1993). This age is later than the ages of 32 Ma in Barckhausen et al. (2014) and ~33 Ma in Li et al. (2014). In the age model of Barckhausen et al. (2014), the initial age was identified from two short magnetic profiles in the northeastern ESB. Nevertheless, the spreading center may have experienced successive southward jumps in this area (described in detail in the next section), which complicates the identification of magnetic anomalies. The incipient age of seafloor spreading from Li et al. (2014) is constrained by the breakup unconformity at Site U1435. Recently, the microfossil dating and analysis of magmatism at Site U1502 from IODP Expeditions 367/368 suggested that the final stage of continental breakup in the ESB occurred at ~30–34 Ma (Larsen et al., 2018). This result supports the initiation of seafloor spreading at ~30 Ma.

Li et al. (2014) proposed that seafloor spreading in the ESB initiated in the northeastern part and then propagated to the west, which is contrary to our observations. In this study, dozens of nearly N–S-trending magnetic profiles cover the entire northern part of the ESB (Figure 1). The identifications of these profiles indicate that seafloor spreading in the ESB contemporaneously initiated at C11n along the eastern and western parts of the northern COB (Figures 2b and 6).

The youngest isochron identified in the ESB is anomaly C5Cr, under the constraints of the microfossil dating of hole U1431 near the fossil ridge. Seafloor spreading in the ESB ceased at ~16 Ma. This cessation age is roughly consistent with the ages estimated by Briais et al. (1993) and Li et al. (2014) but later than 20.5 Ma presented by Barckhausen et al. (2014).

Our results partially support the age models of Taylor and Hayes (1980, 1983) and Briais et al. (1993), but propose different age interpretations for the oceanic crust in the northeastern ESB and near the fossil ridge. Furthermore, the age model with a higher

409 resolution and greater coverage provides more detailed information for the dynamic
410 processes of seafloor spreading in the SCS, as discussed below.

411 **5.2 Successive ridge jumps and asymmetry of the oceanic crust**

412 The geometry of the ESB exhibits an asymmetry with a smaller area on the south
413 flank of the fossil ridge (Figure 2). Especially in the eastern part, the north flank has
414 accreted ~450 km of oceanic crust from the fossil ridge to the northern COB, which is
415 1.5 times that of the south flank. Moreover, the magnetic anomalies on both flanks also
416 show distinct asymmetry in amplitudes and numbers from C6Cr to COB (Figure 3).
417 The geometric and magnetic asymmetry is thought to be the result of ridge jumps
418 (Briais et al., 1993; Ding et al., 2018).

419 We present a successive ridge jump pattern to explain the distinct geometric and
420 magnetic asymmetry (Figures 3 and 6). In this pattern, three ridge jumps occurred
421 during the early spreading stage. The first ridge jump occurred in the eastern part at ~28
422 Ma (C9r) and jumped southward by ~30 km, which left the paired magnetic lineations
423 C10r on the present-day north flank (Figure 6b). This ridge jump was a synchronous
424 reorientation involving minor clockwise rotation (Figures 5a and 6b). Ding et al. (2018)
425 identified two conjugate lower crustal reflector groups from a multichannel seismic
426 transect in the eastern part, which may support this ridge jump. The second ridge jump
427 occurred in the eastern part at ~26 Ma (C8n) and jumped southward by ~42 km. The
428 paired magnetic lineations C8r were left on the present-day north flank (Figure 6c). The
429 third ridge jump occurred through the entire ESB at ~25 Ma and jumped southward by
430 ~20 km, leaving the paired magnetic lineations C7r on the present-day north flank
431 (Figure 6d). This ridge jump has also been identified by previous studies (Barckhausen
432 et al., 2014; Briais et al., 1993; Li et al., 2014; Taylor & Hayes, 1983). Although these
433 ridge jumps are only observed in the northern ESB, they may also have occurred
434 simultaneously in a large area in the east of the SCS that has subducted beneath the
435 Philippine sea plate.

The three southward ridge jumps caused a total distance difference of approximately 184 km between the two flanks from C6Cr to COBs in the eastern part and left magnetic lineations C10r–C7r on the present-day north flank. Meanwhile, successive ridge jumps eliminated a ~70 km-long offset between the eastern and western parts and aligned magnetic lineation C6r across the entire ESB (Figure 6).

Successive ridge jumps are usually ascribed to the effects of hot spots or plumes on ridges (Brozena et al., 1990; Mittelstaedt et al., 2011; Müller et al., 1998). More ridge jumps could occur in young plates with slow spreading rates (Mittelstaedt et al., 2011). However, there is no clear evidence of plumes beneath the SCS and the spreading rates during the jumping are also intermediate spreading rates (~49-64 mm/yr) (Figure 5b). In other regions away from hot spots or plumes, ridge jumps during the initiation of seafloor spreading have also been observed (Benes et al., 1997; d'Acremont et al., 2010; Taylor et al., 1999, 2009). Analyzing the evolution of the spreading segments in these regions, Taylor et al. (2009) suggested that ridge jumps are common processes that reorganize ridge orientation. When the ridge jumps at C9r and C8n occurred in the SCS, the corresponding spreading direction rotated by 9° and 8.5°, respectively (Figure 5a). Although the spreading direction at C7n has not been calculated, the strike of the spreading ridge rotated from the NWW–SEE-trending at C7r to the nearly E-W-trending at C6Cr (Figures 2 and 3), indicating that the spreading direction also changed slightly when ridge jump occurred at C7n. Therefore, the successive ridge jumps may result from the frequent reorientation of seafloor spreading in the SCS, which reflects the instability of the dynamic processes of the basin during the early spreading stage.

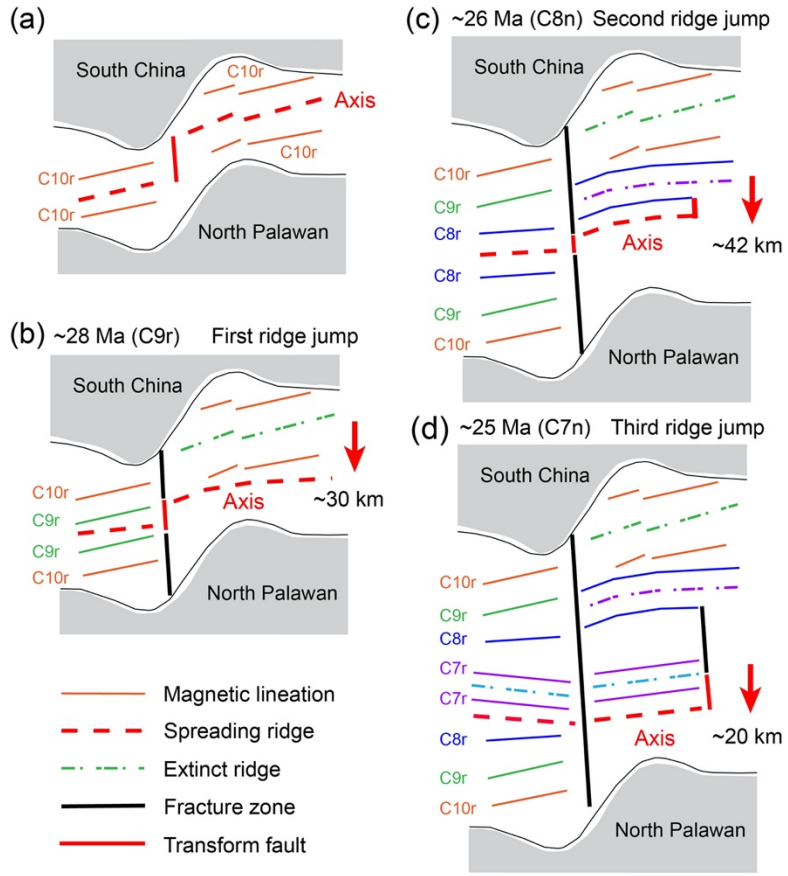

459

460 **Figure 6**. Schematic diagram of successive ridge jumps during the early spreading
461 stage.

462 **5.3 Rotations of the spreading direction and fracture zones**

463 The continuous counterclockwise rotations of seafloor spreading in the SCS
464 reorganized the orientation and segmentation of the spreading ridge. From C6Cr to
465 C5Dr, the counterclockwise rotations caused a ~13° change in the spreading direction.
466 The slow and/or relatively small rotation resulted in a gradual rotation and segmentation
467 of the spreading ridge. The spreading ridge gradually rotated from nearly E–W at C6Cr
468 to NEE–SWW at C5Er and was broken into several segments connected by small
469 transform faults (Figures 2 and 7). The gradual ridge rotation is a typical reorientation
470 type, which occurred repeatedly in the north-eastern Pacific and Shikoku–Parece Vela
471 Basins (Kasuga & Ohara, 1997; Menard & Atwater, 1968; Okino et al., 1999). At C5Dr,
472 a significant counterclockwise rotation caused a ~37° change in the spreading direction.
473 The larger and more rapid rotation resulted in the spreading ridge reorientation by a

synchronous jump. The reoriented spreading ridges (C5Dr) obliquely intersect the existing seafloor and the abandoned spreading center. Similar processes also occurred in the recent spreading stage of the Woodlark Basin (Goodliffe et al., 1997).

The transform faults between the spreading ridge segments formed a series of fracture zones with seafloor spreading. These fracture zones record the changes in the spreading direction and seafloor spreading history of the SCS. However, the locations and trends of the fracture zones are still unclear because they are covered by 1-2 km of sediment (Ruan et al., 2016). The negative VGG anomaly could provide information for the sediment-covered fracture zones (Hwang & Chang, 2014; Sandwell et al., 2014) and can be compared with the fracture zones depicted by the flowlines (Pitman & Talwan, 1972). Therefore, we calculate synthetic flowlines based on the stage poles and attempt to determine the fracture zones by comparing it with the VGG, outcropping geomorphic features, and magnetic anomalies.

The Zhongnan fracture zone, the boundary of the ESB with the SWSB and NWSB, is the most important fracture zone in the SCS, and its formation throughout the entire opening period of the SCS. The negative VGG anomaly shows that the Zhongnan fracture zone between the ESB and the NWSB is nearly N–S-trending along approximately 115.7°E before C10r, NNW–SSE-trending between C10r and C9r, and then extends southward along the COB on the northeast of Zhongsha Islands after C9r (Figure 7b). The changes of the fracture zone trend are consistent with the evolution of the spreading direction (Figure 5a). The offset in the lineation C6Cr near 115.9°E and continuous lineation C6Br indicate the fracture zone extending southward terminated before C6Br. Further west, a young fracture zone began to form at C7r, with the westward propagation of seafloor spreading. From C7r to C5Dr, the fracture zone extended southward along approximately 115.5°E and is slightly concave to the east. The concave corresponds to gradual counterclockwise rotation in the spreading direction between C6Cr and C5Dr. After C5Dr, the trend of the fracture zone rotated suddenly to NW–SE-trending shown by the negative VGG anomaly, geomorphic

features, and magnetic anomalies. The prominent rotation is associated with the major counterclockwise rotation in the spreading direction at C5Dr (Figure 5a). At the same time, a synchronous ridge jump occurred with counterclockwise rotation. The jump caused the Zhongnan fracture zone in the north flank to be elongated by ~40 km and that in the south flank to be shorten by the same distance. The flowlines are adjusted based on the jump and indicate that the Zhongnan fracture zone in the south flank locates on the west of the outcropping ridge and extends along the ridge southward to COB (Figure 7a). The location of the fracture zone is also supported by the magnetic lineations C6Cr with conjugated small offsets (Figure 7c). Therefore, the Zhongnan fracture zone may be a discontinuous fracture zone, which is composed of the fracture zone before C6Br and the subsequent S-shaped fracture zone. To the east, we also identify two additional fracture zones resulted from the reorientation and segmentation of the spreading ridge (Figure 7).

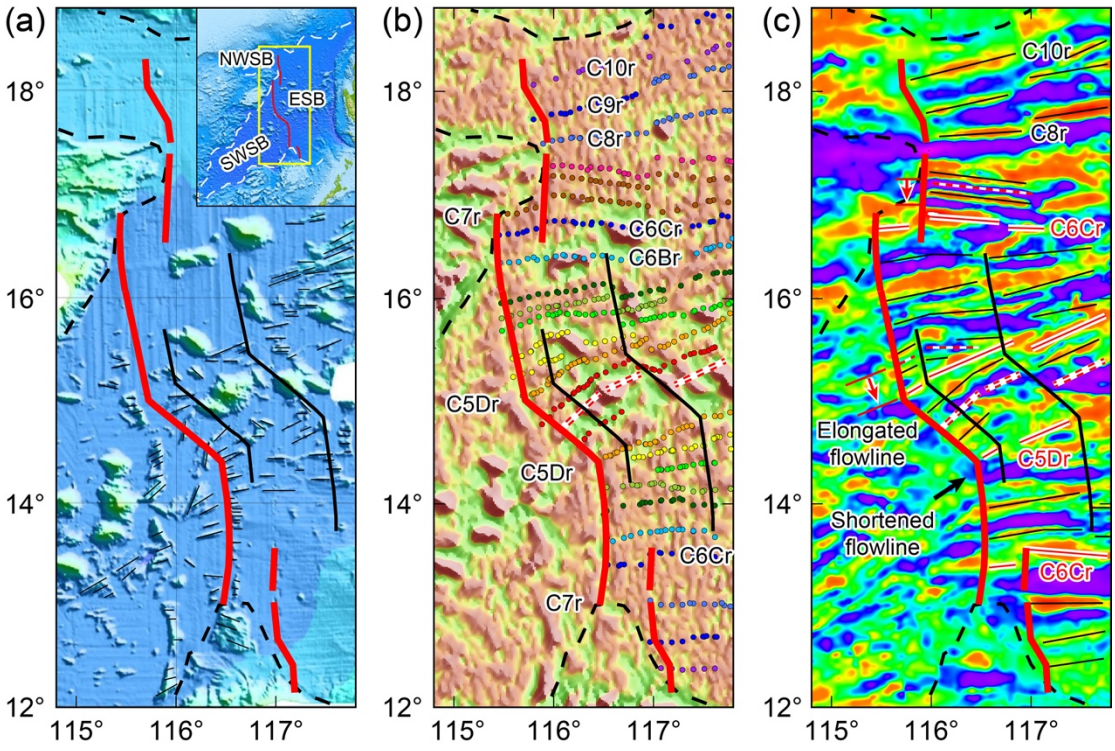

Figure 7. (a) Bathymetric map located in the central part of the South China Sea (SCS). Short black lines indicate outcropping seafloor spreading lineaments. (b) Vertical gravity gradient map (Sandwell et al., 2014) with the magnetic picks. (c) Magnetic

anomalies map with the magnetic lineations. Thick red lines indicate the Zhongnan fracture zone. Thin black lines indicate two fracture zones parallel to the Zhongnan fracture zone. Red dashed lines indicate the locations of the ridge jump.

5.4 Dynamic processes of the evolution of the SCS

Spreading ridge jumps and rotations are common processes that reorganize the orientation of ridges in marginal basins, such as the Woodlark Basin (Goodliffe et al., 1997; Taylor et al., 2009), the Shikoku–Parece Vela Basin (Kasuga & Ohara, 1997; Okino et al., 1999). The occurrence of these processes is a response to changes in plate motion around the basins (Goodliffe et al., 1997). Similarly, seafloor spreading of the SCS, located at the junction of three major plates, may have also been potentially associated by the surrounding plates and microplates tectonics. The ages of many spreading processes in the SCS were coeval with the tectonic events of the surrounding plates. For example, an instantaneous ridge jump occurred at 25 Ma, which coincided with the period of the most important Cenozoic plate boundary reorganization. In this period, the southward extrusion of Indochina block along the EVBFZ ceased (Fyhn et al., 2009a, 2009b), the Ontong Java Plateau collided with the Melanesian Arc, and the northern Australian margin collided with the southern Philippine plate (Hall, 2002; Hall et al., 1995). The termination of seafloor spreading in the SCS at ~16 Ma was coeval with the collision of the Dangerous Grounds–Reed Bank microcontinents and northern Borneo (Holloway, 1982; Hutchison et al., 2000). The significant counterclockwise rotations of seafloor spreading in the SCS at ~18 Ma also coincided with the termination of Indochina block left-lateral movements along the ARRSZ (Leloup et al., 1993). However, Indochina block was extruded southward along the EVBFZ on the west of the SCS, and the extrusion along the EVBFZ terminated at ~25 Ma (Fyhn et al., 2009a, 2009b). Hall (2002) suggested that subduction-related controls are far more important than other processes in most parts of Southeast Asian and West Pacific. Moreover, the spreading pattern in the Shikoku–Parece Vela Basin caused by the oblique subduction of the Pacific plate is very similar to that in the SCS. Therefore, we tentatively discuss

547 the possible causes for the counterclockwise rotations of seafloor spreading in the SCS
548 based on the main framework of the slab pull models and surrounding plate tectonics.
549 In this model, the PSCS slab subducted southward beneath the Borneo, while
550 Borneo rotated counterclockwise by ~50° between 25 Ma and 10 Ma (Fuller et al.,
551 1999). As the rotation of Borneo, the amount of subducted slab increased from the west
552 to the east along the subduction zone (Sibuet et al., 2016). A greater slab pull may have
553 arisen in the eastern subduction zone because the net slab pull force increases with the
554 amount of subducted slab (Schellart, 2004) (Figure 8), which could cause the south
555 flank of the SCS to drift southeastward. By 20 Ma to 15 Ma, the initial subduction of
556 the eastern SCS beneath the western Philippine plate may have further provided space
557 for the eastward component of the south flank drift and triggered the prominent
558 counterclockwise rotation of the spreading direction of the SCS at 18 Ma (C5Dr)
559 (Figure 8). Therefore, the combined effect of the changes in the direction of the PSCS
560 slab pull and the SCS slab subduction beneath the Philippine plate could be a possible
561 explanation for the counterclockwise rotation of seafloor spreading in the SCS.

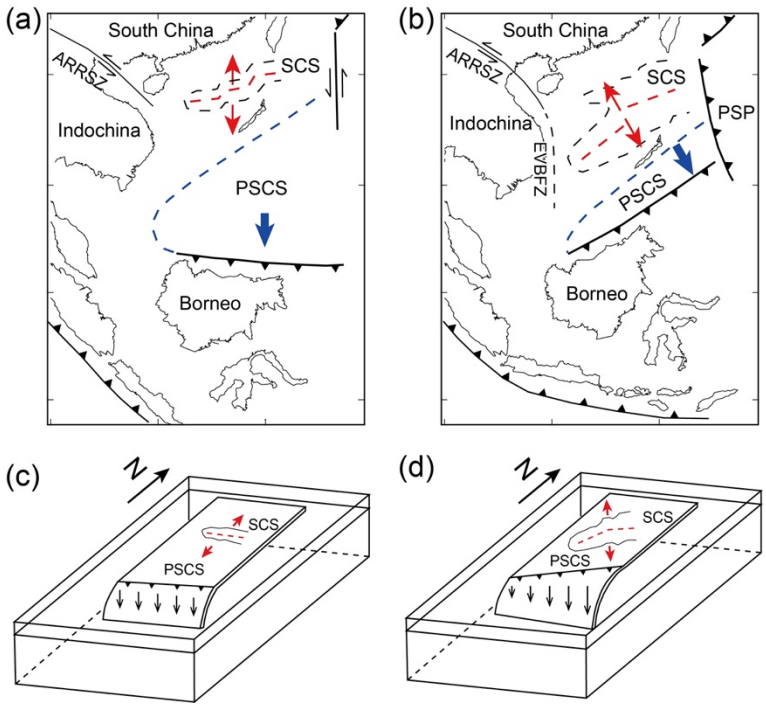

562

Figure 8. Structural sketch of the study area. (a) The PSCS subducted southward during the early spreading stage of the SCS. (b) The subduction direction of the PSCS gradually changed to the southeast, with the counterclockwise rotation of Borneo. (c) and (d) are schematic models of (a) and (b), respectively. ARRSZ, Ailaoshan-Red River Shear Zone. EVBFZ, East Vietnam Boundary Fault Zone. PSP, Philippine Sea Plate.

6 Conclusions

We reinterpreted the magnetic anomalies in the ESB based on the new marine magnetic dataset and present a high-resolution crustal age model. Age model shows that seafloor spreading initiated contemporaneously along the eastern and western parts of the COB at ~30 Ma (C11n) and ceased at ~16 Ma (C5Br). The average full spreading rate of the ESB is 53 mm/yr, which is an intermediate spreading rate.

During the early spreading stage, three ridge jumps occurred at C9r, C8n, and C7n, resulting in the distinct geometric and magnetic asymmetry of the ESB. A synchronous ridge jump with counterclockwise rotation occurred at C5Dr, obliquely intersecting the existing seafloor and the abandoned spreading center. After C6Cr, the seafloor spreading continuously rotated counterclockwise, reorganizing the segmentation of the spreading ridge and forming a series of S-shaped fracture zones.

Successive spreading ridge jumps and continuous rotations of seafloor spreading are important features in the opening processes of the SCS, which may have been associated with the surrounding plate tectonics. We speculate that the counterclockwise rotations of seafloor spreading may be related to the changes in the direction of the PSCS slab pull and the eastward subduction of the SCS.

Acknowledgments

We appreciate the helpful discussions with Fan Zhang, Zhiyuan Zhou, Chunguo Yang, Zhaocai Wu, and Zhongyan Shen. This research was supported by the National Nature Science Foundation of China (grant 41890811, grant 41976079, grant 41576065, and grant 40776036), the National Program on Global Change and Air-Sea Interaction (GASI-GEOGE-05), and the National Major Scientific Instruments and Equipment Development Project of China (2014YQ100817-06). We used the Modmag software (Mendel et al., 2005) and GPlates software (Müller et al., 2018) in this work. Most of the figures were made using the GMT software (Wessel et al., 2019). The magnetic picks are available from https://github.com/QingshengGuan/SCS-Magnetic-picks.git.

595 **References**

596 Barckhausen, U., Engels, M., Franke, D., Ladage, S., & Pubellier, M. (2014). Evolution
597 of the South China Sea: Revised ages for breakup and seafloor spreading. *Marine and*
598 *Petroleum Geology, 58*, 599-611. doi:10.1016/j.marpetgeo.2014.02.022

599 Barckhausen, U., & Roeser, H. A. (2004). Seafloor spreading anomalies in the South
600 China Sea revisited. In P. Clift, W. R. Kuhnt, P. Wang, & D. Hayes (Eds.), *Continent-*
601 *ocean interactions within East Asian marginal seas, Geophysical Monograph Series*
602 (Vol. 149). Washington, DC: American Geophysical Union.

603 Benes, V., Bocharova, N., Popov, E., Scott, S., & Zonenshain, L. (1997). Geophysical
604 and morpho-tectonic study of the transition between seafloor spreading and continental
605 rifting, western Woodlark Basin, Papua New Guinea. *Marine Geology, 142*(1), 85-98.
606 doi:10.1016/S0025-3227(97)00042-X

607 Briais, A., Patriat, P., & Tapponnier, P. (1993). Updated interpretation of magnetic
608 anomalies and seafloor spreading stages in the South China Sea: implications for the
609 Tertiary tectonic of Southeast Asia. *Journal of Geophysical Research, 98*(B4), 6299-
610 6328. doi:10.1029/92JB02280

611 Brozena, J. M., & White, R. S. (1990). Ridge jumps and propagations in the South
612 Atlantic Ocean. *Nature, 348*(6297), 149-152. doi: 10.1038/348149a0

613 Chang, T. (1988). Estimating the Relative Rotation of Two Tectonic Plates from
614 Boundary Crossings. *Journal of the American Statistical Association, 83*(404), 1178-
615 1183. doi:10.1080/01621459.1988.10478717

616 d'Acremont, E., Leroy, S., Maia, M., Gente, P., & Autin, J. (2010). Volcanism, jump
617 and propagation on the Sheba ridge, eastern Gulf of Aden: segmentation evolution and
618 implications for oceanic accretion processes. *Geophysical Journal International,*
619 *180*(2), 535-551. doi:10.1111/j.1365-246X.2009.04448.x

620 Ding, W., Sun, Z., Dadd, K., Fang, Y., & Li, J. (2018). Structures within the oceanic
621 crust of the central South China Sea basin and their implications for oceanic
622 accretionary processes. *Earth and Planetary Science Letters, 488*, 115-125.
623 doi:10.1016/j.epsl.2018.02.011

624 Ding, W., Sun, Z., Mohn, G., Nirrengarten, M., Tugend, J., Manatschal, G., & Li, J.
625 (2019). Lateral evolution of the rift-to-drift transition in the South China Sea: Evidence
626 from multi-channel seismic data and IODP Expeditions 367&368 drilling results. *Earth*
627 *and Planetary Science Letters, 531*. doi:10.1016/j.epsl.2019.115932

628 Fan, C., Xia, S., Zhao, F., Sun, J., Cao, J., Xu, H., & Wan, K. (2017). New insights into
629 the magmatism in the northern margin of the South China Sea: Spatial features and
630 volume of intraplate seamounts. *Geochemistry, Geophysics, Geosystems, 18*(6), 2216-
631 2239. doi:10.1002/2016gc006792

632 Fuller, M., Ali, J. R., Moss, S. J., Frost, G. M., Richter, B., & Mahfi, A. (1999).
633 Paleomagnetism of Borneo. *Journal of African Earth Sciences, 17*(1-2), 3-24.
634 doi:10.1016/S0743-9547(98)00057-9

635 Fyhn, M. B. W., Boldreel, L. O., & Nielsen, L. H. (2009a). Geological development of
636 the Central and South Vietnamese margin: Implications for the establishment of the
637 South China Sea, Indochinese escape tectonics and Cenozoic volcanism.
638 *Tectonophysics, 478*(3-4), 184-214. doi:10.1016/j.tecto.2009.08.002

639 Fyhn, M. B. W., Nielsen, L. H., Boldreel, L. O., Thang, L. D., Bojesen-Koefoed, J.,
640 Petersen, H. I., . . . Abatzis, I. (2009b). Geological evolution, regional perspectives and
641 hydrocarbon potential of the northwest Phu Khanh Basin, offshore Central Vietnam.
642 *Marine and Petroleum Geology, 26*(1), 1-24. doi:10.1016/j.marpetgeo.2007.07.014

643 Gao, J. Y., & Liu, B. H. (2014). *China's offshore ocean–marine geophysics*. Beijing:
644 China Ocean Press.

Gee, J. S., & Kent, D. V. (2007). Source of oceanic magnetic anomalies and the geomagnetic polarity timescale. In G. Schubert (Ed.), *Treatise on geophysics* (Vol. 5, pp. 455-507). Amsterdam: Elsevier.

Gilley, L. D., Harrison, T. M., Leloup, P. H., Ryerson, F. J., Lovera, O. M., & Wang, J.-H. (2003). Direct dating of left-lateral deformation along the Red River shear zone, China and Vietnam. *Journal of Geophysical Research: Solid Earth, 108*(B2). doi:10.1029/2001jb001726

Goodliffe, A. M., Taylor, B., Martinez, F., Hey, R., Maeda, K., & Ohno, K. (1997). Synchronousre orientation of the Woodlark Basin Spreading Center. *Earth and Planetary Science Letters, 146*, 233-242. doi:10.1016/S0012-821X(96)00227-0

Hall, R. (2002). Cenozoic geological and plate tectonic evolution of SE Asia and the SW Pacific: computer-based reconstructions, model and animations. *Journal of African Earth Sciences, 20*(4), 353-431. doi:10.1016/S1367-9120(01)00069-4

Hall, R., Ali, J. R., Anderson, C. D., & Baker, S. J. (1995). Origin and motion history of the Philippine SeaPlate. *Tectonophysics, 251*(1-4), 229-250. doi:10.1016/0040-1951(95)00038-0

Hellinger, S. J. (1981). The uncertainties of finite rotations in plate tectonics. *Journal of Geophysical Research: Solid Earth, 86*(B10), 9312-9318. doi:10.1029/JB086iB10p09312

Holloway, N. H. (1982). North Palawan Block, Philippines–Its relation to Asian mainland and role in evolution of South China Sea. *The American Association of Petroleum Geologists Bulletin, 66*(9), 1355-1383.

Hsu, S.-K., Armada, L. T., Yeh, Y.-C., Dimalanta, C. B., Tsai, C.-H., & Bacolcol, T. (2019). The seafloor fabrics and evolution of a propagated rift system in the South China Sea: 2019 AGU Fall Meeting, T43F-0508.

Hutchison, C. S., Bergman, S. C., Swauger, D. A., & Graves, J. E. (2000). A Miocene collisional belt in north Borneo: uplift mechanism and isostatic adjustment quantified by thermochronology. *Journal of the Geological Society, 157*(4), 783-793. doi:10.1144/jgs.157.4.783

Hwang, C., & Chang, E. T. (2014). Geophysics. Seafloor secrets revealed. *Science, 346*(6205), 32-33. doi:10.1126/science.1260459

Kasuga, S., & Ohara, Y. (1997). A new model of back-arc spreading in the Parece Vela Basin, northwest Pacific margin. *The Island Arc, 6*(3), 316-326. doi:10.1111/j.1440-1738.1997.tb00181.x

Koppers, A. P. (2014). On the $^{40}Ar/^{39}Ar$ dating of low-potassium ocean crust basalt from IODP Expedition 349, South China Sea: 2014 AGU Fall Meeting, T31E-03.

Larsen, H. C., Mohn, G., Nirrengarten, M., Sun, Z., Stock, J., Jian, Z., . . . Zhong, L. (2018). Rapid transition from continental breakup to igneous oceanic crust in the South China Sea. *Nature Geoscience, 11*(10), 782-789. doi:10.1038/s41561-018-0198-1

Leloup, P. H., Arnaud, N., Lacassin, R., Kienast, J. R., Harrison, T. M., Trong, T. T. P., . . . Tapponnier, P. (2001). New constraints on the structure, thermochronology, and timing of the Ailao Shan-Red River shear zone, SE Asia. *Journal of Geophysical Research: Solid Earth, 106*(B4), 6683-6732. doi:10.1029/2000jb900322

Leloup, P. H., Harrison, T. M., Ryerson, F. J., Wenji, C., Qi, L., Tapponnier, P., & Lacassin, R. (1993). Structural, petrological and thermal evolution of a Tertiary ductile strike-slip shear zone, Diancang Shan, Yunnan. *Journal of Geophysical Research: Solid Earth, 98*(B4), 6715-6743. doi:10.1029/92jb02791

Li, C. F., Lin, J., Kulhanek, D. K. & Expedition 349 Scientists. (2015). Expedition 349 summary. In Proc. IODP (eds Li, C.-F., Lin, J., Kulhanek, D. K. & Expedition 349 Scientists) Vol. 349. doi:10.14379/iodp.proc.349.101.2015

695 Li, C. F., Xu, X., Lin, J., Sun, Z., Zhu, J., Yao, Y. J., . . . Zhang, G. L. (2014). Ages and
696 magnetic structures of the South China Sea constrained by deep tow magnetic surveys
697 and IODP Expedition 349. *Geochemistry Geophysics Geosystems, 15*, 4958-4983.
698 doi:10.1002/2014GC005567

699 Li, J. B., Ding, W. W., Wu, Z. Y., Zhang, J., & Dong, C. Z. (2012). The propagation of
700 seafloor spreading in the southwestern subbasin, South China Sea. *Chinese Science*
701 *Bulletin, 57*(24), 3182-3191. doi:10.1007/s11434-012-5329-2

702 Li, J. B., Jin, X. L., & Gao, J. Y. (2002). Tectonic and geomorphological study of the
703 South China Sea in the late spreading stage. *Science in China (Series D), 32*(3), 239-
704 248. doi:10.3969/j.issn.1674-7240.2002.03.009

705 Menard, H. W., & Atwater, T. (1968). Changes in direction of sea floor spreading.
706 *Nature, 219*(5153), 463-467. doi: 10.1038/219463a0

707 Mendel, V., Munschy, M., & Sauter, D. (2005). MODMAG, a MATLAB program to
708 model marine magnetic anomalies. *Computers & Geosciences, 31*(5), 589-597.
709 doi:10.1016/j.cageo.2004.11.007

710 Mittelstaedt, E., Ito, G., & van Hunen, J. (2011). Repeat ridge jumps associated with
711 plume-ridge interaction, melt transport, and ridge migration. *Journal of Geophysical*
712 *Research, 116*(B1). doi:10.1029/2010jb007504

713 Müller, R. D., Cannon, J., Qin, X., Watson, R. J., Gurnis, M., Williams, S., . . .
714 Zahirovic, S. (2018). GPlates: Building a Virtual Earth Through Deep Time.
715 *Geochemistry, Geophysics, Geosystems, 19*(7), 2243-2261.
716 doi:10.1029/2018gc007584

717 Müller, R. D., Roest, W. R., & Royer, J.-Y. (1998). Asymmetric seafloor spreading
718 caused by ridge-plume interactions. *Nature, 396*(6710), 455-459. doi:10.1038/24850

719 Nirrengarten, M., Mohn, G., Schito, A., Corrado, S., Gutiérrez-García, L., Bowden, S.
720 A., & Despinois, F. (2020). The thermal imprint of continental breakup during the

721 formation of the South China Sea. *Earth and Planetary Science Letters, 531*.
722 doi:10.1016/j.epsl.2019.115972

723 Okino, K., Ohara, Y., Kasuga, S., & Kato, Y. (1999). The Philippine Sea: New survey
724 results reveal the structure and the history of the marginal basins. *Geophysical Research*
725 *Letters, 26*(15), 2287-2290. doi:10.1029/1999gl900537

726 Pitman, W. C., & Talwan, M. (1972). Sea-Floor Spreading in the North Atlantic.
727 *Geological Society of America Bulletin, 83*(3), 619-646. doi:10.1130/0016-
728 7606(1972)83[619:SSITNA]2.0.CO;2

729 Ruan, A. G., Wei, X. D., Niu, X. W., Zhang, J., Dong, C. Z., Wu, Z. L., & Wang, X. Y.
730 (2016). Crustal structure and fracture zone in the Central Basin of the South China Sea
731 from wide angle seismic experiments using OBS. *Tectonophysics*.
732 doi:10.1016/j.tecto.2016.09.022

733 Sandwell, D. T., Müller, R. D., Smith, W. H. F., Garcia, E., & Francis, R. (2014). New
734 global marine gravity model from CryoSat-2 and Jason-1 reveals buried tectonic
735 structure. *Science, 346*(6205), 65-67. doi:10.1126/science.1258213

736 Schärer, U., Tapponnier, P., Lacassin, R., Leloup, P. H., Zhong, D., & Ji, S. C. (1990).
737 Intraplate tectonics in Asia: a precise age for large-scaleMiocene movement along the
738 Ailao Shan-Red River shear zone, China. *Earth and Planetary Science Letters, 97*(1),
739 65-77. doi:10.1016/0012-821X(90)90099-J

740 Schellart, W. P. (2004). Quantifying the net slab pull force as a driving mechanism for
741 plate tectonics. *Geophysical Research Letters, 31*(7). doi:10.1029/2004gl019528

742 Sibuet, J. C., Yeh, Y. C., & Lee, C. S. (2016). Geodynamics of the South China Sea.
743 *Tectonophysics, 692*, 98-119. doi:10.1016/j.tecto.2016.02.022

744 Sun, Z., Jian, Z., Stock, J. M., Larsen, H. C., Klaus, A., Alvarez Zarikian, C. A., & the
745 Expedition 367/368 Scientists. (2018). Proceedings of the International Ocean
746 Discovery Program Volume 367/368. doi:10.14379/iodp.proc.367368.101.2018

747 Tapponnier, P., Lacassin, R., Leloup, P. H., Schärer, U., Dalai, Z., Haiwei, W., . . .
748 Jiayou, Z. (1990). The Ailao Shan/Red River metamorphic belt: Tertiary left-lateral
749 shear between Indochina and South China. *Nature, 343*(6257), 431-437.
750 doi:10.1038/343431a0

751 Tapponnier, P., Peltzer, G., Le Dain, A. Y., Armijo, R., & Cobbold, P. (1982).
752 Propagating extrusion tectonics in Asia: New insights from simple experiments with
753 plasticine. *Geology, 10*(12). doi:10.1130/0091-7613(1982)10<611:Petian>2.0.Co;2

754 Taylor, B., Goodliffe, A., & Martinez, F. (1999). How continents break up: Insights
755 from Papua New Guinea. *Journal of Geophysical Research: Solid Earth, 104*(B4),
756 7497-7512. doi:10.1029/1998jb900115

757 Taylor, B., Goodliffe, A., & Martinez, F. (2009). Initiation of transform faults at rifted
758 continental margins. *Comptes Rendus Geoscience, 341*(5), 428-438.
759 doi:10.1016/j.crte.2008.08.010

760 Taylor, B., & Hayes, D. E. (1980). The tectonic evolution of the South China Basin. In
761 D. E. Hayes (Ed.), *The Tectonic and Geologic Evolution of Southeast Asian Seas and*
762 *Islands: Part 1* (Vol. 23, pp. 89-104). Washington, DC: American Geophysical Union.

763 Taylor, B., & Hayes, D. E. (1983). Origin and History of the South China Sea Basin.
764 In D. E. Hayes (Ed.), *The Tectonic and Geologic Evolution of Southeast Asian Seas*
765 *and Islands: Part 2, Geophysical Monograph Series* (Vol. 27, pp. 23-56). Washington,
766 DC: American Geophysical Union.

767 Thébault, E., Finlay, C. C., Beggan, C. D., Alken, P., Aubert, J., Barrois, O., . . . Zvereva,
768 T. (2015). International Geomagnetic Reference Field: the 12th generation. *Earth,*
769 *Planets and Space, 67*(1), 79. doi:10.1186/s40623-015-0228-9

770 Tozer, B., Sandwell, D. T., Smith, W. H. F., Olson, C., Beale, J. R., & Wessel, P. (2019).
771 Global Bathymetry and Topography at 15 Arc Sec: SRTM15+. *Earth and Space*
772 *Science, 6*(10), 1847-1864. doi:10.1029/2019ea000658

773 Wessel, P., Luis, J. F., Uieda, L., Scharroo, R., Wobbe, F., Smith, W. H. F., & Tian, D.
774 (2019). The Generic Mapping Tools Version 6. *Geochemistry, Geophysics, Geosystems,*
775 *20*(11), 5556-5564. doi:10.1029/2019gc008515

776 Wu, J., Suppe, J., Lu, R., & Kanda, R. (2016). Philippine Sea and East Asian plate
777 tectonics since 52 Ma constrained by new subducted slab reconstruction methods.
778 *Journal of Geophysical Research: Solid Earth, 121*(6), 4670-4741.
779 doi:10.1002/2016jb012923

780 Yao, B. C. (1995). Characteristics and tectonic significance of Zhongnan-Liyue fault.
781 *Geological Research of South China Sea (in Chinese)*, 7.

782 Zahirovic, S., Seton, M., & Müller, R. D. (2014). The Cretaceous and Cenozoic tectonic
783 evolution of Southeast Asia. *Solid Earth, 5*(1), 227-273. doi:10.5194/se-5-227-2014

784 Zhang, T., Dyment, J., & Gao, J. Y. (2019). Age of the Canada basin, Arctic Ocean:
785 indications from high-resolution magnetic data. *Geophysical Research Letters, 46*(23),
786 13712-13721. doi:10.1029/2019gl085736

787 Zhang, T., Gao, J. Y., Li, J. B., WU, Z. C., Wu, Z. L., Zhao, L. H., . . . Zhou, Z. Y.
788 (2012). The magnetic lineation identifications and segmentation of the northwestern
789 sub-basin in the South China Sea. *Chinese Journal of Geophysics-Chinese Edition,*
790 *55*(9), 3163-3172. doi:10.6038/j.isn.0001-5733.2012.09.034